Black phosphorus based fiber optic biosensor for ultrasensitive cancer diagnosis

Zhou, Lin; Liu, Chen; Sun, Zhengbo; Mao, Hongju; Zhang, Lin; Yu, Xuefeng; Zhao, Jianlong; Chen, Xianfeng

Biosensors and Bioelectronics

DOI:
10.1016/j.bios.2019.04.044

Published: 15/07/2019

Peer reviewed version

Black phosphorus based fiber optic biosensor for ultrasensitive cancer diagnosis

Lin Zhou[a,b], Chen Liu[a], Zhengbo Sun[c], Hongju Mao[b], Lin Zhang[d], Xuefeng Yu[c], Jianlong Zhao[b], Xianfeng Chen[a,*]

[a] *School of Computer Science and Electronic Engineering, Bangor University, Bangor LL57 1UT, United Kingdom*
[b] *State Key Laboratory of Transducer Technology, Shanghai Institute of Microsystem and Information Technology, Chinese Academy of Sciences, Shanghai 200050, China*
[c] *Institute of Biomedicine and Biotechnology, Shenzhen Institutes of Advanced Technology, Chinese Academy of Sciences, Shenzhen 518055, China*
[d] *Aston Institute of Photonic Technologies, Aston University, Birmingham B4 7ET, United Kingdom*

ABSTRACT

We propose the first black phosphorus (BP) – fiber optic biosensor for ultrasensitive diagnosis of human neuron-specific enolase (NSE) cancer biomarkers. A novel optical-nano configuration has been exploited by integrating BP nanosheets with a largely tilted fiber grating (BP-TFG), where the BP is bio-functionalized by the poly-L-lysine acting as a critical cross-linker to facilitate bio-nano-photonic interface with extremely enhanced light-matter interaction. BP nanosheets are synthesized by a liquid ultrasonication-based exfoliation and deposited on fiber device by an in-situ layer-by-layer method. The BP-induced optical modulation effects in terms of thickness-tunable feature, polarization-dependence and enhanced light-matter interaction are experimentally investigated. The anti-NSE immobilized BP-TFG biosensor has been implemented to detect NSE biomarkers demonstrating ultrahigh sensitivity with limit of detection down to 1.0 pg/mL, which is 4 orders magnitude lower than NSE cut-off value of small cell lung cancer. The enhanced sensitivity of BP-TFG is 100-fold higher than graphene oxide or AuNPs based biosensors. We believe that BP-fiber optic configuration opens a new bio-nano-photonic platform for the applications in healthcare, biomedical, food safety and environmental monitoring.

Keywords: Black phosphorus; Optical biosensor; Fiber grating; Label-free; Neuron-specific enolase; Cancer biomarker

1. Introduction

2D-layered materials have attracted enormous attention due to their extraordinary mechanical, electronic, optical and chemical properties (Novoselov et al., 2004; Geim, 2009; Huang et al., 2013). Various nanomaterials including graphene, transition metal dichalcogenides (TMDs) and boron/carbon nitride have been developed for widespread applications in electronics, optical modulators, energy storages and sensors (Sun et al., 2016; Bonaccorse et al., 2010; Loh et al., 2010). However, the intrinsic shortcomings such as the lack of bandgap in graphene and the lower carrier mobility in molybdenum disulfide limit their utilities. As a new member of 2D materials family, 2D-layered black phosphorus (BP) has triggered renaissance of research interest since its first mechanical exfoliation from bulk BP in 2014 (Reich, 2014; Li et al., 2014; Xia et al., 2014; Liu et al., 2014). BP has a puckered lattice configuration along the armchair direction and a bilayer structure along the zigzag direction. BP consists of corrugated planes of phosphorus atoms with strong in-plane covalent bonding and weak interlayer van der Waals interactions. Due to the unique puckered orthorhombic structure and in-plane anisotropy, BP possesses much higher surface-to-volume ratio, extremely large hole mobility, and superior molecular adsorption energy which surpass those of other 2D materials (Reich, 2014; Li et al., 2014). As a new class of 2D materials, BP has a layer-dependent bandgap ranging from ~0.3 eV for bulk to ~2.0 eV for monolayer (Liu et al., 2014), which can bridge the gap between the gapless graphene and large bandgap TMDs (Kim et al., 2015; Rodin et al., 2014). Although numerous investigations have been conducted to study the optoelectronic properties and applications of BP, little attention has been paid to its potential biomedical applications. This might be mainly due to the lack of biocompatibility of BP hence low biological activities upon exposure to biological environment with small biomolecules and low concentrations (Li et al., 2015; Abbas et al., 2015; Sun et al., 2015; Hanlon et al., 2016; Kumar et al., 2016; Shao et al., 2016).

Neuron-specific enolase (NSE) is a highly specific cancer biomarker that has been detected in patients with certain tumors, such as neuroendocrine tumor, lung cancer, medullary thyroid cancer, carcinoid tumors, endocrine tumors of the pancreas, and melanoma (Isgro et al., 2015). Usually, the concentration of the biomarker secreted to the blood stream by

* Corresponding author. School of Computer Science and Electronic Engineering, Bangor University, Bangor LL57 1UT, United Kingdom
Email address: x.chen@bangor.ac.uk (X. Chen).

tumors in their early stages of growth is very low, therefore it remains a challenge to develop a sensitive method to detect the biomarkers. Determination of NSE levels in clinical practice can provide information about tumor burden, number of metastatic sites and response to the treatment. Small cell lung cancer (SCLC) has been noted for high malignance, short doubling time, early metastasis, easy recurrence and high mortality (Van Meerbeeck et al., 2011). NSE is currently the most reliable tumor biomarker in diagnosis, prognosis and follow-up of SCLC (Isgro et al., 2015; Van Meerbeeck et al., 2011). NSE is used to provide quantitative measures to identify SCLC, with the cut-off value of 15.2 ng/mL in clinical diagnosis (Wang et al., 2013).

The recent exploitation reveals that 2D-layered materials could modulate light with superior performance for realistic applications in ultrafast laser, light processing, chemical and biomedical applications (Sun et al., 2016; Liu et al., 2014). Bao et al. reported the use of atomic layer graphene as saturable absorber for ultrafast pulsed fiber laser and in-line fiber-to-graphene coupler for the broadband polarizer (Bao et al., 2009; Bao et al., 2011). Albert et al. demonstrated gold nanofilm-coated tilted fiber grating (TFG) as a plasmonic sensor and gold nanoparticles (AuNPs) based optical fiber sensor for protein detection (Caucheteur et al., 2016; Lepinay et al., 2014). With the advancement of material science and lab-on-fiber technology (Cusano et al., 2014; Wang and Wolfbeis, 2013), various materials including thin metal film, carbon nanotubes, titanium dioxide, zinc oxide, graphene and graphene oxide (GO) have been deposited on short-period fiber gratings and long-period gratings (LPGs) for the enhancement of performance (Erdogan, 1997; Zhou et al., 2006; James and Tatam, 2013; Del Villar et al., 2005; Coelho et al., 2016). Among those materials, the large surface area of 2D-layered materials maximize the effect of adsorbed molecules on the host layer resulting in high sensitivity (Tan et al., 2014; Jiang et al., 2016; Liu et al., 2017; Liu et al., 2018). The use of fiber based optical biosensing platform takes the intrinsic merits of the optical fibers, such as electromagnetic interference immunity, compactness, lightness, and high compatibility with optoelectronic devices. Moreover, in-fiber grating technology provides advantages of high sensitivity, real-time, multiplexing and in-line determination as the optical signal is spectrally modulated (Cusano et al., 2014; Wang and Wolfbeis, 2013; Chiavaioli et al., 2017). However, the lack of biocompatibility and coating approach restricts the usage of BP for fiber optic biosensing and biomedical applications (Choi et al., 2018).

In this paper, for the first time to our knowledge, we propose a BP-fiber optic biosensor for ultrasensitive diagnosis of NSE cancer biomarker. As illustrated in Fig. 1, a largely tilted fiber grating acting as optical transducer couples the light from fiber core to cladding yielding evanescent field at cladding/surrounding boundary. BP nanosheets are synthesized by a liquid-phase exfoliation method and deposited on the fiber by an in-situ layer-by-layer (i-LbL) technique. BP overlay is biofunctionalized by poly-L-lysine (PLL) to provide a biocompatible environment for the immobilization of anti-NSE, leaving active binding sites free for bioaffinity recognition of target NSE biomarkers. The perturbation caused by affinity binding changes local analyte concentration hence local refractive index (RI), alerting the optical signal which can be monitored in real-time as a change of local RI, thereby eliminating the need of ligand labeling. The BP-TFG has been implemented to detect the specific human NSE biomarkers as well as non-specific biomolecules, demonstrating ultrahigh sensitivity, specificity, real-time, and label-free sensing performance.

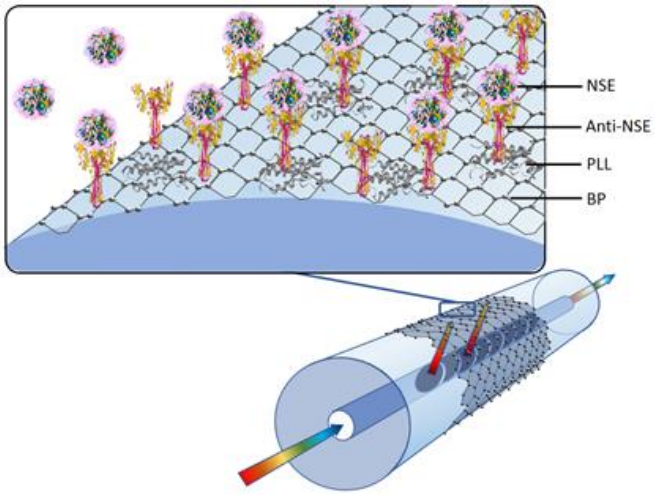

Fig. 1. Schematic of biofunctionalized black phosphorus based optical biosensing platform. The BP nanosheets deposited tilted fiber grating (BP-TFG) provides an ultrasensitive bioanalytical platform for the detection of affinity interactions between bioreceptor anti-NSE and target NSE biomarkers.

2. Materials and methods

2.1. Materials

The (3-Aminopropyl)triethoxysilane (APTES), Sodium hydroxide (NaOH), Poly-L-lysine (PLL), N-(3-Dimethylaminopropyl)-N′-ethylcarbodiimide hydrochloride (EDC), N-Hydroxysuccinimide (NHS), Phosphate buffered saline (1×PBS, pH 7.4), Bovine serum albumin (BSA), immunoglobulin G (IgG) and prostate specific antigen (PSA) were purchased from Sigma-Aldrich (United Kingdom). Anti-Human neuron-specific enolase (anti-NSE) was purchased from Medix Biochemica Inc. (Finland). Human neuron-specific enolase (NSE) was purchased from Abcam Ltd. (United Kingdom). Isopropanol, methanol, ethanol, acetone, and deionized (DI) water were purchased from Thermo Fisher Scientific Inc. (United Kingdom).

All chemical and biochemical reagents were of analytical grade and were used as received without further purification. All aqueous solutions were prepared with DI water.

2.2. Fabrication of largely tilted fiber grating

The 82°-TFG with grating length of 8 mm was inscribed in a hydrogenated BGe single mode fiber by the use of a frequency-doubled Ar laser at 244 nm wavelength and mask scanning technique. After UV fabrication, the TFG was annealed at 80°C

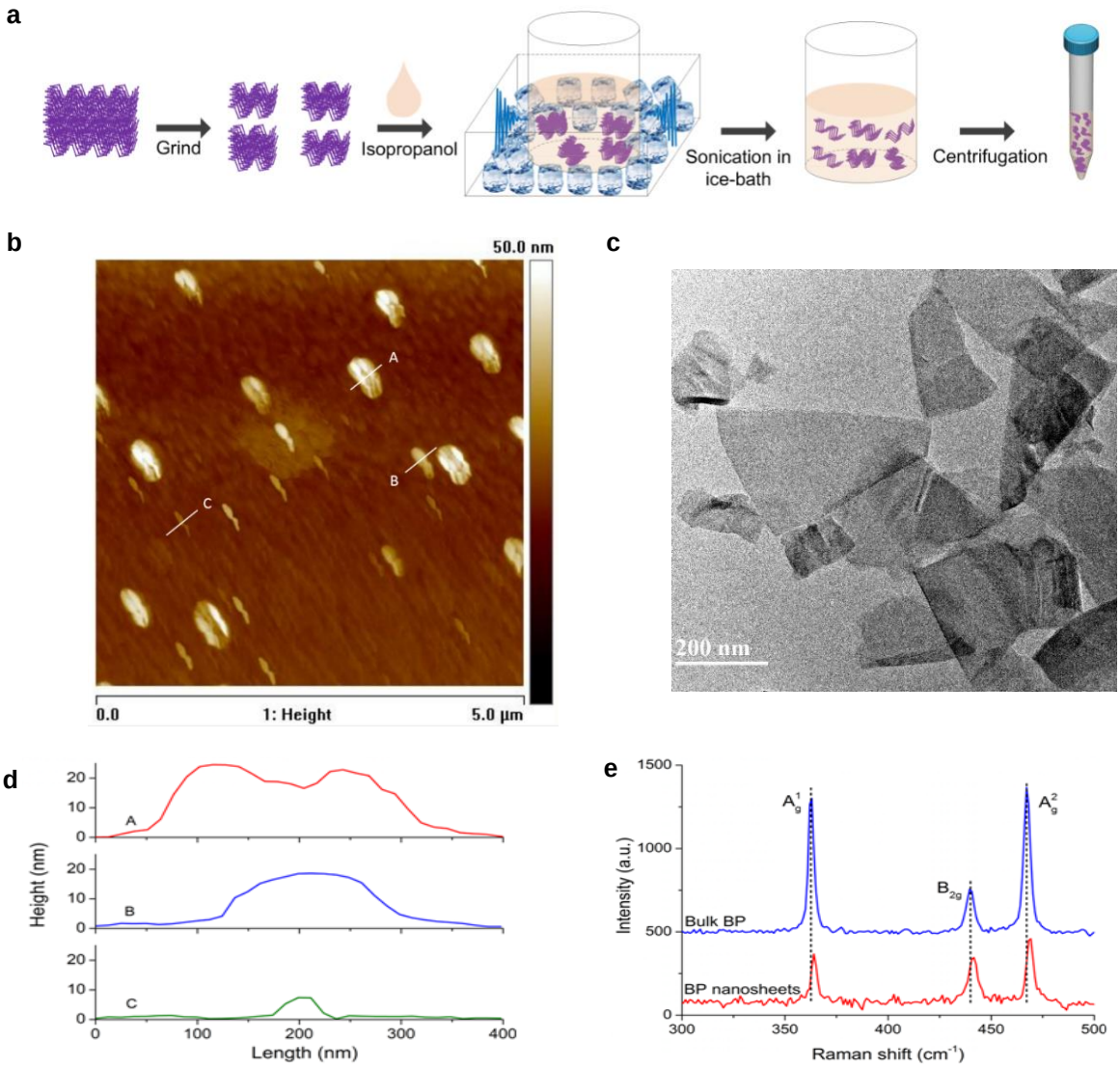

Fig. 2. BP nanosheets synthesis and characterization. (a) Schematic illustration of BP nanosheets synthesis with liquid ultrasonication-based exfoliation. (b) AFM image of BP nanosheets. (c) TEM image of BP nanosheets. (d)The corresponding height profiles (A, B, C) of three measured BP nanosheets in (b) along the white lines. (e) Raman spectra of bulk BP and BP nanosheets.

for 48 h to remove the residual hydrogen and to stabilize the optical properties.

2.3. BP nanosheets synthesis and characterization

Similar to our previous work (Sun et al., 2015), BP nanosheets were synthesized by the use of liquid ultrasonication-based exfoliation of bulk BP in solvent, which was replaced by isopropanol in this work. As shown in Fig. 2a, the bulk BP was grinded into small pieces then dissolved by 25 mL isopropanol. Subsequently, the BP dispersion was sonicated in an ultrasonic bath operating at 25 kHz 1200 W power for 3 h to break the van der Waals stack of BP, where the temperature was maintained below 277 K by the use of ice. After sonication, the as-prepared solution was centrifuged at 5000 rpm for 15 min to remove the residual un-exfoliated BP. In final, the supernatant liquid containing few-layered BP nanosheets was collected for further usage.

Atomic force microscopy (AFM) was used to characterize the liquid-exfoliated BP nanosheets (Fig. 2b). The BP nanosheets owned terraces of different thickness features, which were widely found in liquid-exfoliated 2D materials (Hanlon et al., 2016). Typically, the individual nanosheets were observed to include regions of different thickness, often with the thicker at the center and thickness decreasing at the edges of the nanosheet, which were partly due to restacking with small nanosheets aggregating on the surface of large nanosheets. As shown in Fig. 2d, the size of BP nanosheets was from several ten nanometers to several hundred nanometers and the thickness was around 7.3 nm to 23.8 nm. As the thickness of BP monolayer was ~0.9 nm (Kumar et al., 2016), which suggested that the BP nanosheets in this work contained 8~26 atomic layers. In further, the transmission electron microscopy (TEM) was used to characterize the detailed morphology of the BP nanosheets obtained. As shown in Fig. 2c, the BP nanosheets are very thin and ca. 200~500 nm in lateral size.

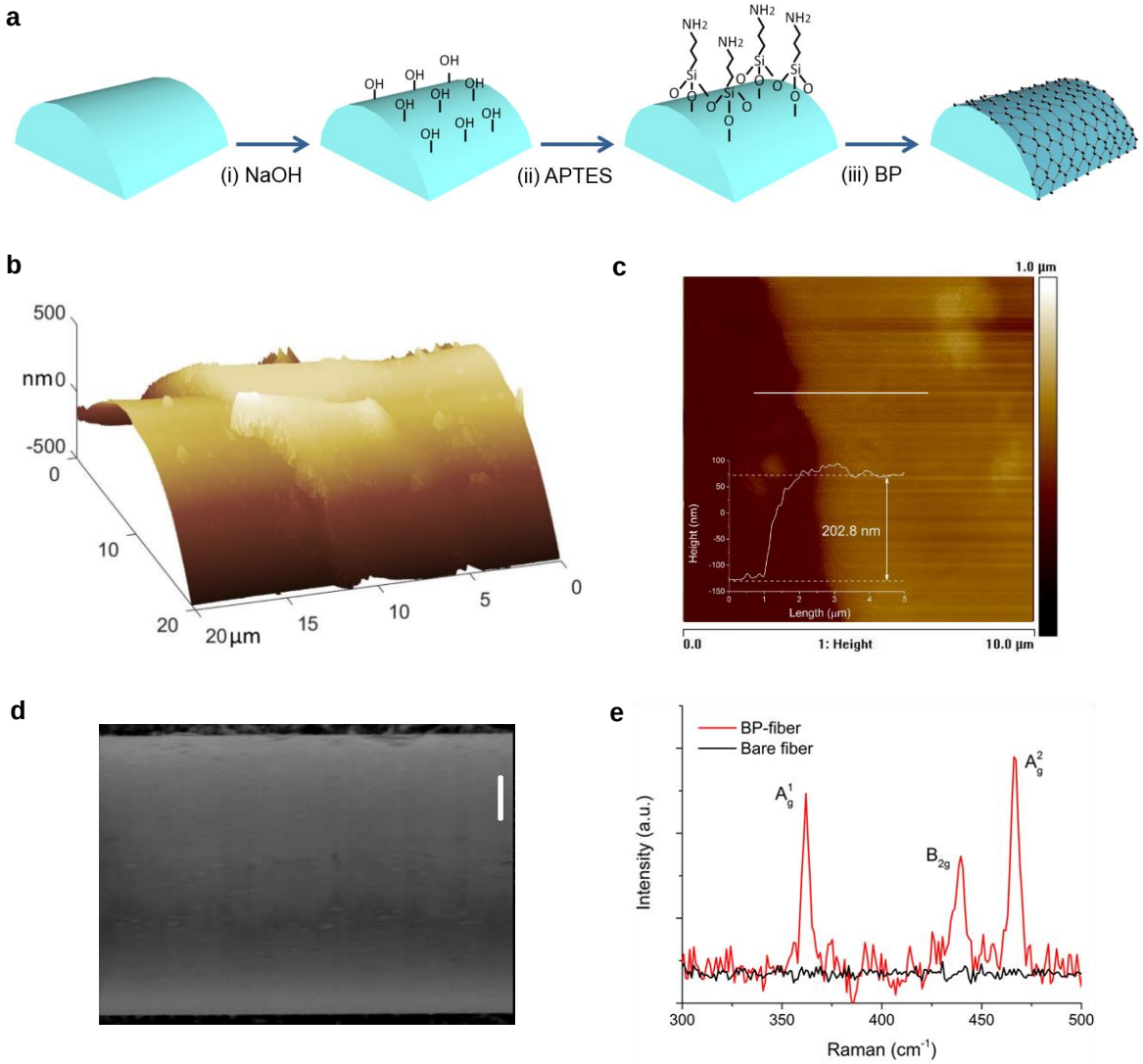

Fig. 3. BP nanosheets deposition on fiber and surface morphology. (a) Schematic diagram of BP deposition: (i) Alkaline treatment for silica fiber surface, (ii) Silanization by APTES, (iii) BP multi-cycle deposition. (b) 3D view of AFM image of BP-coated cylindrical fiber with step boundary. (c) 2D AFM micrograph with the height profile (inset) extracted along the white line. (d) SEM image of BP overlay on fiber surface (scale bar: 20 µm). (e) Raman spectra of BP-coated fiber and bare fiber.

Raman spectra (Fig. 2e) of bulk BP and BP nanosheets reveal the bands at 362.0, 439.6, 467.1 cm^{-1} assigned to A_g^1 , B_{2g} and A_g^2 three characteristic peaks corresponding to BP materials, indicating BP nanosheets preserve the structure of bulk BP. The A_g^1 corresponds to atoms oscillate out-of-plane while B_{2g} and A_g^2 relate to atoms vibrate within the plane. Due to the ultrathin thickness of the exfoliated nanosheets, the Raman spectrum of BP nanosheets shows slightly shift toward high wavenumber compared with bulk BP (Dhanabalan et al., 2017).

2.4. BP deposition on cylindrical fiber

Transferring nano-film or depositing 2D-layered nanosheets on non-planar substrate is a big challenge. We developed an in-situ layer-by-layer deposition technique based on chemical-bonding associated with physical-adsorption (Liu et al., 2017). In this work, we used the freshly exfoliated BP nanosheets therefore the BP nanosheets had very good stability and dispersibility.

As illustrated in Fig. 3a, the section of fiber over the grating region was rinsed with acetone for 30 min to remove the organic contaminants and washed with DI water thoroughly and dried. Subsequently, (i) an alkaline treatment was conducted by immersing the fiber device in 1.0 M NaOH solution for 1 h at room temperature then washed with DI water to enrich the number of hydroxyl (-OH) groups on fiber surface; (ii) a silanization procedure was followed by incubating the fiber into a freshly-prepared 5% (v/v) APTES ethanol solution for 1 h at room temperature, which mainly reacted with hydroxyl groups to form Si-O-Si bonding yielding a positively charged surface, then the fiber was washed with ethanol to remove unbound monomers and baked in an oven at 70 °C for 30 min to enhance the stability of APTES monolayer; (iii) the APTES-silanized fiber was kept straightly in a custom-made microchannel container where 30 µL BP isopropanol solution was added to

immerse the fiber device. Upon solvent evaporation and drying, the negatively charged BP nanosheets were gradually bonded on the positively charged fiber surface. After 30 min when the solvent fully evaporated, the second cycle was implemented by carefully pipetting 30 µL BP nanosheets solution into microchannel container to cover the fiber. When the solvent was evaporating, BP nanosheets were being gradually adsorbed on the fiber surface. Such evaporating and drying processes enhanced the physisorption between BP nanosheets and fiber surface. After five cycles of deposition, the BP-coated TFG was placed in a vacuum drying oven at 40 °C for 12 h to enhance the adhesion between BP nanosheets and fiber and to improve the uniformity of BP overlay.

2.5. Measurement system and data analysis

Renishaw Raman Microscope 1000 (with 632.8 nm light) was employed to characterize Raman spectra of BP material. The thickness of BP nanosheets and BP deposited overlay were measured by AFM (Veeco Instruments Inc., di Dimension 3100). The surface coverage of BP-fiber was measured by SEM (Hitachi, S-520).

For optical interrogation system, broadband light source (BBS: Agilent HP83437A, Agilent Technologies Inc.) was used along with an optical spectrum analyzer (OSA, Agilent HP86142A, Agilent Technologies Inc.). The OSA was connected to a computer and the optical spectra were recorded by a customized program. Data analysis was performed using the customized program which automatically defined resonance wavelength using the centroid calculation method.

All biochemical procedures were performed in a fume cupboard. To minimize the cross-sensitivities of temperature and bend, all experiments were conducted at a controlled room temperature of 22.0 ± 0.1 °C unless specified otherwise, and the fiber device was placed straightly in a custom-made microchannel container and all the chemicals and solvents were added and withdrawn by careful pipetting.

3. Results and discussion

3.1. BP-fiber surface morphological characterization

The surface morphological characterization was verified by AFM, SEM and Raman spectroscopy. As shown in AFM tapping mode topographic images (Fig. 3b and c), an overlay has been successfully deposited on the cylindrical fiber surface where a step boundary is clearly presented between bare and coated- sections. The height profile (inset in Fig. 3c) gives the BP overlay thickness of ~202.8 nm after five coating cycles. The surface was further examined by SEM (Fig. 3d) to show a homogeneous coating over entire cylindrical fiber surface demonstrating a high-quality deposition. Raman spectra (Fig.

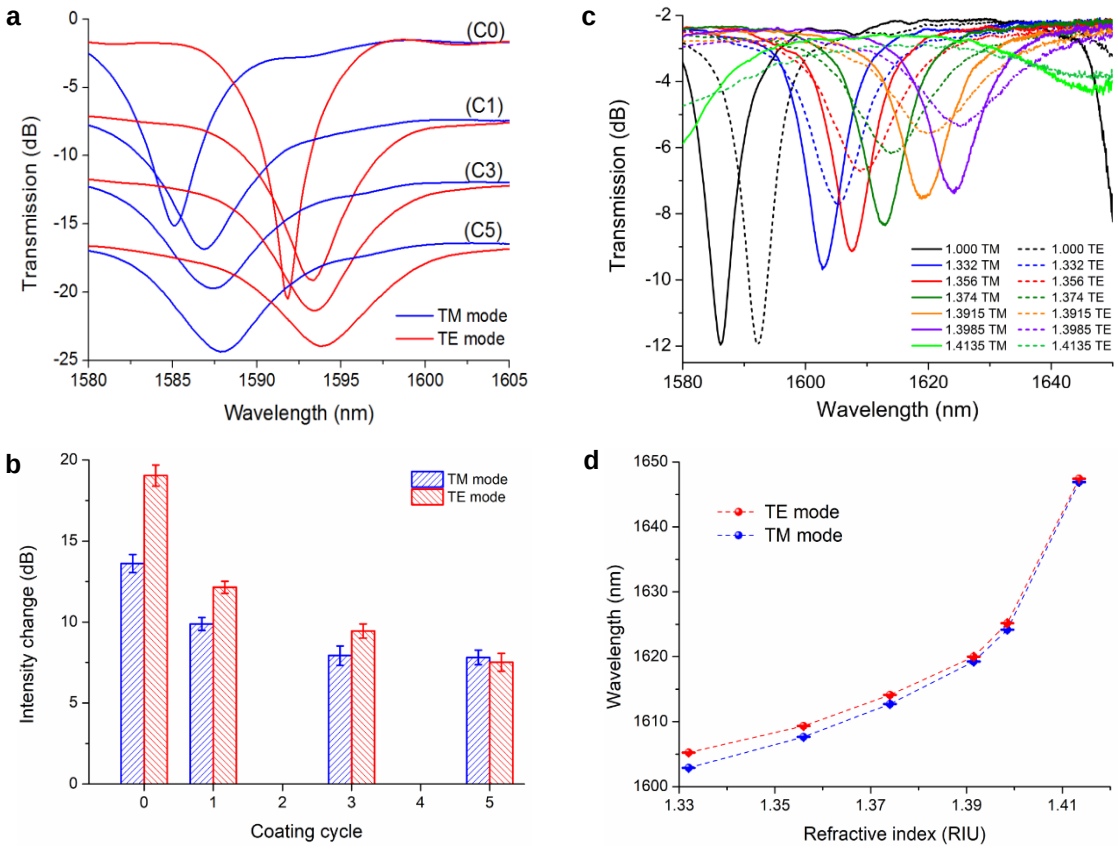

Fig. 4. BP-induced strong optical modulation and enhanced light-matter interaction. (a) TFG spectral evolution during BP deposition processes (C0: non-coating, C1-C5: after coating 1st, 3rd, and 5th cycle, respectively). (b) Intensity change of different polarization peaks. (c) Transmission spectra of BP-TFG in different RI medium. (d) Wavelength shift against external RI.

3e) confirm that the overlay is BP as its spectrum after the deposition maintaining the same characteristic peaks as BP nanosheets.

The developed i-LbL deposition technique secured high-quality nano-coating deposited on non-planar substrate with strong adhesion as well as a precise thickness control. By taking the flexibility of i-LbL approach, the overlay thickness can be precisely controlled by adjusting the deposition conditions, such as dispersion concentration, quantity, number of coating cycles, evaporation time, or their combination.

3.2. BP-induced strong optical modulation and enhanced light-matter interaction

Due to the birefringence caused by the largely titled fringes in fiber core, the 82°-TFG exhibits intrinsic optical polarization properties. When the light is launched into fiber core and experiences the largely tilted structures, it is coupled to the forward-propagating cladding modes which appear two sets of comb-like split resonances in transmission spectra at discrete wavelengths given by the following phase-matching conditions (Erdogan, 1997):

$$\lambda_{co-cl} = \left(n_{co,i}^{eff} - n_{cl,m}^{eff}\right) \cdot \frac{\Lambda_g}{cos\theta} \quad (1)$$

where $n_{co,i}^{eff}$ is the effective refractive index of fiber core, i represents transverse-magnetic (TM) or transverse-electric (TE) polarization state, $n_{cl,m}^{eff}$ is the m^{th} effective refractive index of cladding, Λ_g is the normal grating period, and θ is the tilted angle of grating.

An 8 mm-long 82°-TFG was UV-inscribed in a BGe single mode fiber. Fig. S1(a) shows an optical image of 82°-tilted fringes by the use of a high magnification microscope with oil immersion. Fig. S1(b) depicts the transmission spectra of 82°-TFG exhibiting two sets of comb-like polarization resonances. With the randomly polarized light launched, both sets exhibited ~3 dB loss (~50%) as the light was equally coupled to two orthogonal birefringence modes. When the input light was linearly polarized in either the tilt plane or perpendicular to it, the comb-like cladding mode resonances became predominantly polarized radially or azimuthally with fully coupled strength.

The light-matter interaction has been significantly enhanced by BP deposition with different BP thickness. The optical properties were observed by monitoring the TFG transmission spectra in real-time during multi-cycle BP deposition. As plotted in Fig. 4a, both TM- and TE- modes demonstrate the trends with red-shift in wavelength and decrease in intensity while BP overlay thickness increased during the coating process. As shown in Fig. 4b, TE resonant intensity weakens 11.53 dB which is 216% larger than that of TM mode after five coating cycles (with BP overlay thickness of ~202.8 nm), where the value of coefficient of variation of intensity change at different cycles for TM and TE mode is between 0.03 and 0.07. During the same process, the TE resonant wavelength shifts 2.12 nm, which is only 75% that of TM mode (Fig. S2). It should be emphasized that different effects between two orthogonal modes indicate BP-induced polarization-dependent modulation as well as thickness-tunable optical characteristics. By taking the advantage of in-fiber grating configuration, it might provide a versatile and practicable method for the overlay thickness control by simply monitoring the intensity change of grating resonance.

RI sensitivity of BP-TFG was evaluated by immersing the device in a set of aqueous sucrose solutions with RIs ranging from 1.332 to 1.4135. Fig. 4c plots the spectral evolution of BP-TFG against RI. It is a clear appearance of intensity reduction of TM and TE resonances while they both move to long wavelength side with increase of external RI. For BP-TFG, the cladding guided modes are partially radiated to the overlay behaving as leaky modes. By increasing external RI, the leaky radiation could reduce the coupling coefficient between core and cladding hence decrease the resonant intensity while the effective RI of cladding could be changed resulting in wavelength shift with respect to the phase-matching condition Eq. (1). It can be seen from Fig. 4d that the RI sensitivity exhibits a nonlinear characteristic and increases dramatically. The RI sensitivities of TM resonance (blue symbols) achieve 198.3 nm/RIU, 373.7 nm/RIU, and 1515.3 nm/RIU for low (1.332-1.356), medium (1.374-1.391) and high (1.398-1.413) RI regions, respectively, while those of TE mode (red symbols) are 170.0 nm/RIU, 336.6 nm/RIU and 1483.3 nm/RIU for the corresponding RI regions. The value of coefficient of variation of wavelength shift at different RI is on the order of 10^{-6}. TM resonance shows higher RI sensitivity than that of TE mode, hence it has been selected for further biosensing experiments. As bioassays and biological events are usually carried out in low RI region (~1.33), it is noteworthy that RI sensitivity of BP-TFG in low RI region is seven times higher than that of the conventional LPGs (Lee 1997), indicating BP-TFG could be a good candidate for biosensing applications. In addition, TFG owns narrow band resonance giving higher Q-factor (~343) and higher accuracy than LPG (Zhou et al., 2006).

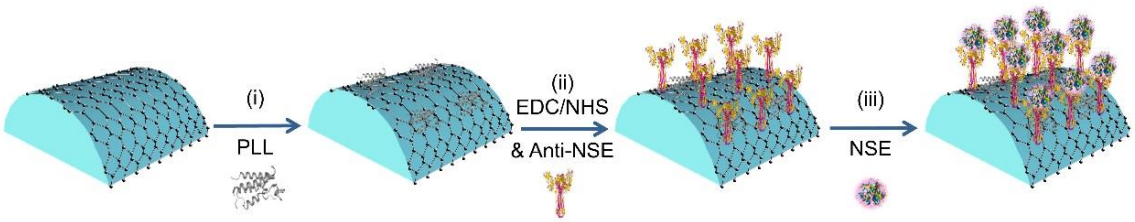

Fig. 5. Biofunctionalization and bioconjugation of BP-TFG. (i) Biofunctionalization with biocompatible PLL, (ii) Immobilization of anti-NSE via EDC/NHS bioconjugation, (iii) Bioaffinity binding between anti-NSE and target NSE biomarkers.

3.3. Biofunctionalization of BP and immobilization of anti-NSE

Construction of bio-nano-photonic interface is a critical role for optical biosensor. It has been reported that poly-L-lysine has various advantages including plentiful active amino groups, flexible molecular backbone, and good biocompatibility and solubility (Kumar et al., 2016; Shan et al. 2009). Functionalization of nanomaterials by biocompatible PLL, as a cross-linker through amide groups, can facilitate the active treatment and provide the opportunities for bioactive molecular attachment.

Fig. 5 plots the schematic of biofunctionalization of BP-fiber optic biosensor. (i) The BP-TFG was incubated in 0.01% PLL solution for 4 h at room temperature. The positively charged PLL attached on BP via electrostatic interaction to form a cross-linker between BP and bioactive molecules. (ii) Then 12 mg/mL EDC, 24 mg/mL NHS and 2 mg/mL anti-Human neuron-specific enolase (anti-NSE) were mixed in 1×PBS to activate the carboxyl groups. The PLL-functionalized BP-TFG was incubated in such EDC/NHS/anti-NSE mixture for 2 h to immobilize anti-NSE molecules. EDC/NHS coupled reactions were highly efficient and usually increased the bioconjugation significantly (Hermanson, 2013). The carbodiimide EDC was used to form active ester functionalities with carboxylate groups using the compound NHS. The advantage of adding NHS to EDC reactions was to increase the solubility and stability of the active intermediate, which ultimately reacted with the attacking amine. NHS esters were hydrophilic reactive groups that coupled rapidly with amines on anti-NSE, which were used to react with the amine groups of PLL to form a covalent immobilization of anti-NSE on host BP, leaving the binding sites free for target NSE recognition. (iii) After that, the anti-NSE bound BP-TFG was washed by 1×PBS buffer and immersed into 1% BSA solution for 30 min. The non-bound anti-NSE was washed away by PBS buffer. The unreacted sites on BP surface were passivated by BSA to block the remaining active carboxylic groups and to prevent non-specific adsorption. Here, the anti-NSE immobilized BP-TFG was ready as a biosensor for the detection of target NSE biomarkers.

The optical responses of BP-TFG from surface modification to biofunctionalization were determined by monitoring the TM-mode spectra (Fig. S3). The resonance has been shifted ~1.40 nm, 1.40 nm, 0.46 nm and 0.59 nm after APTES silanization, BP deposition, PLL biofunctionalization, and anti-NSE

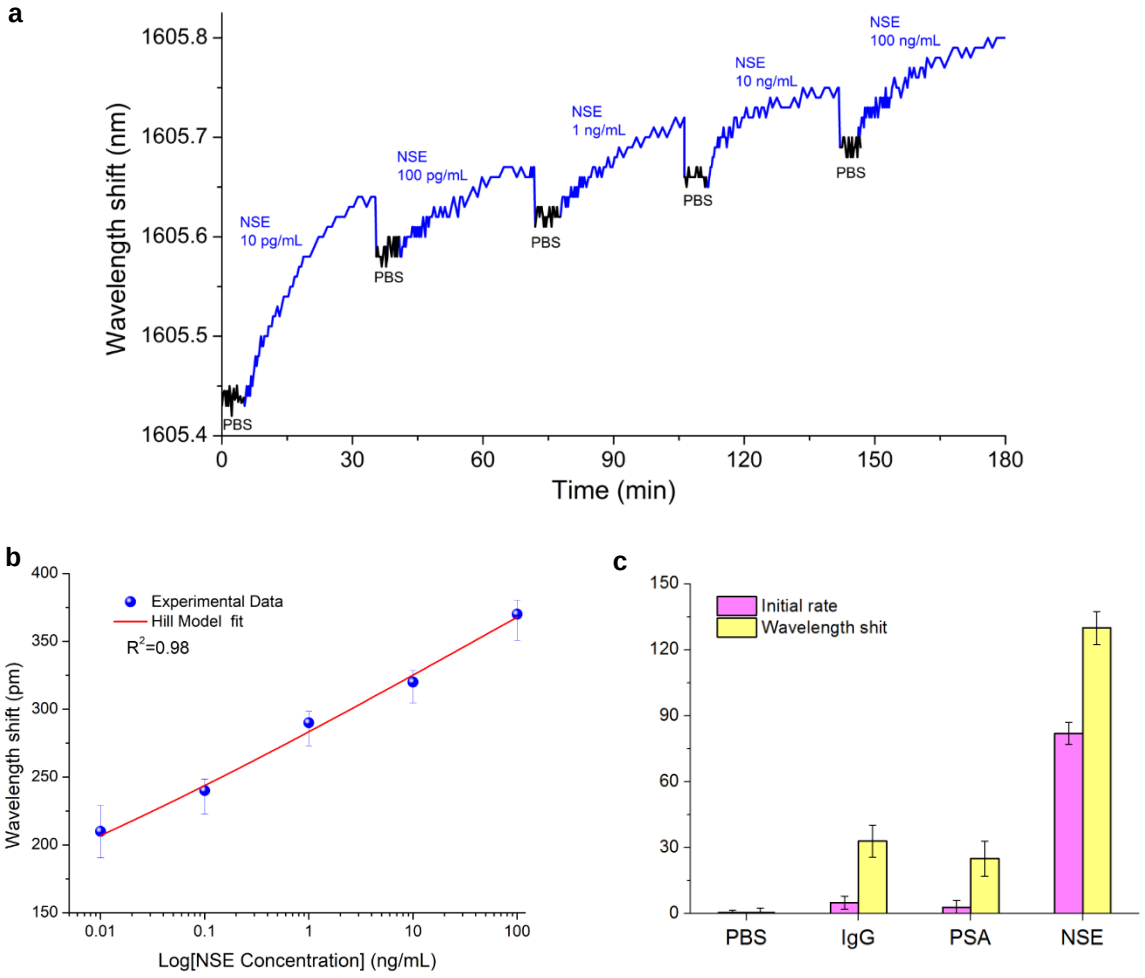

Fig. 6. Label-free detection of NSE with anti-NSE immobilized BP-TFG. (a) Wavelength shift caused by binding interactions with target NSE samples with concentration of 0.01, 0.1, 1.0, 10, and 100 pg/mL, respectively. (b) Dependence of wavelength shift against NSE concentrations. The red line is the best Hill model fit curve. (c) Specificity of BP-TFG biosensor (in PBS, IgG, PSA, and NSE).

immobilization, respectively. Due to the multiple modifications applied on device surface, the effective RI of cladding was modified yielding a total resonant red-shift of 3.85 nm while the leaky radiation reduced the coupling coefficient hence decreased the peak intensity by 5.6 dB.

3.4. Label-free detection of NSE biomarkers

The anti-NSE bound BP-TFG was employed to monitor the kinetic binding interaction between anti-NSE and target NSE biomarkers. Five consecutive binding processes for human NSE sample in 1× PBS buffer solutions with concentration of 0.01, 0.1, 1.0, 10, and 100 ng/mL were detected by monitoring TM resonant wavelength shift in real-time. The PBS buffer (1×PBS, pH 7.4) was firstly used to prewash the device for 5 min, offering a sensing baseline where the spectrum was recorded (Fig. S4-a). Then, the NSE sample solution was applied to immerse the sensor device for 30 min (Fig. S4-b). As depicted in Fig. 6a, the first 5-min was a rapid-state bind process in which the optical signal showed a significant wavelength shift, then the reaction rate began to asymptote to a steady-state for the following 20-min, and gradually achieved saturation-state in the last 5-min. After that, a subsequent rinsing with PBS buffer was followed to wash away the unbound NSE molecules prior to the next measurement. The wavelength shift after deducting the baseline value is 210, 240, 290, 320, and 370 pm for NSE concentration of 0.01, 0.1, 1.0, 10, and 100 ng/mL, respectively. Since the evanescent field penetrating from cladding/BP boundary to the surrounding-medium with the enhanced light-matter interface, even very small local RI change due to the affinity binding would cause an observable wavelength shift.

The wavelength shift as a function of NSE concentration has been plotted in Fig. 6b. The red line provides the best Hill model fitting of the experimental data. Hill model can be described as (Koopal et al., 1994; Nakatsuka et al., 2018):

$$\Delta\lambda = \Delta\lambda_{max}\, C_{NSE}^{n}/(K_d^{n} + C_{NSE}^{n}) \quad (2)$$

where $\Delta\lambda_{max}$ is the maximum wavelength shift of the reaction, K_d is the dissociation constant of the interaction between receptor and ligand molecules, C_{NSE} is the ligand concentration, and n is the Hill coefficient, which is useful for determining the degree of cooperativity of the ligand binding to the receptor. The Hill equation provides a way to quantify the degree of interaction between ligand binding sites. According to Eq. (2), the calculated value of $\Delta\lambda_{max}$, K_d, and n is 718.9 pm, 64.0 ng/mL and 0.10, respectively. The Hill coefficient n is less than 1, indicating the negative cooperativity with respect to ligand binding to the receptor. The molecular weight of NSE is approximately 47 kDa, resulting in a dissociation constant K_d of 1.36×10^{-9} M which agrees with the previous research (Acero Sánchez et al., 2016). Based on the experimental results, the limit of detection (LOD, at a signal/noise ratio of 3) of NSE concentration is calculated below 1.0 pg/mL, which is 4 orders of magnitude lower than NSE cut-off value (15.2 ng/mL) of SCLC (Wang et al., 2013), demonstrating the possibility for quantitative detection of NSE in clinical samples. The enhanced biosensing sensitivity is 100-fold higher than GO- and AuNPs-based biosensors (Zhou et al. 2009; Qu et al., 2011). Due to its ultrahigh surface-to-volume ratio, wide tunable range of bandgap and superior molecular adsorption energy, BP plays an important role as bio-nano-photonic interface which increases the sensing area, number of binding sites, and affinity binding efficiency, hence amplifies the optical signal providing superior biosensing performance.

For the practical biosensing application, the reusability is an important function. The reusability of the proposed BP-TFG has been examined by detecting the binding interaction in 10 ng/mL NSE for multiple times. Fig. S5 presents the comparison results for three cycles with the percentages of resonant wavelength shift and initial binding rate. The maximum wavelength shift as the absolute RI change after reducing the baseline signal in PBS prewashing stage retained 95.5% and 91.5% after second and third cycle, respectively. Likewise, the initial binding rate calculated with the data over the first 3 min of binding interaction maintained greater than 89% and 88.5% after second and third cycle, respectively. These results confirmed that the BP-TFG biosensor could be used to detect the NSE/anti-NSE binding for multiple times.

3.5. Specificity of BP-TFG biosensor

The specificity of the biosensor was evaluated to detect the non-specific analytes such as IgG, PSA and PBS in comparison with the specific target NSE, all at a same concentration of 10 ng/mL. During the detection processes, the optical signal was monitored in real-time and recorded (Fig. S6). The comparison results are presented in Fig. 6c, showing the specificity evaluation with the initial reaction rate of the first 3-min and the maximum signal change over whole process. The initial rates for PBS, IgG and PSA were 0%, 6%, 3% that of NSE, while the maximum wavelength shifts for PBS, IgG and PSA were 0%, 25%, 19% that of NSE, respectively. This indicates that the proposed biosensor shows a strong preference for the specific affinity binding of NSE, demonstrating sufficient selectivity for NSE detection.

4. Conclusion

We proposed the first BP-fiber optic biosensor for ultrasensitive diagnosis of NSE cancer biomarkers. BP nanosheets were synthesized and deposited on fiber device to enhance the light-matter interaction where the unique optical modulation effects induced by BP were experimentally observed. The PLL-biofunctionalized BP provided a remarkable analytical platform for affinity binding interface. The BP-TFG was implemented to detect NSE biomarkers demonstrating an ultrahigh sensitivity with the LOD of 1.0 pg/mL, which is 4 orders magnitude lower than NSE cut-off value of SCLC. The enhanced sensitivity is 100-fold higher than GO- or AuNPs- based biosensors. The capability of BP-fiber optic biosensor with ultrahigh sensitivity and specificity opens up the possibility for early diagnosis of cancer, tumor and diseases. In order to match the requirements of practical application, the performance of BP-TFG biosensor will be evaluated with the clinical samples in the future work.

Acknowledgements

The authors acknowledge support from the projects of EU FP7 PIRSES-GA-2013-612267 (iPhoto-Bio, European Commission); the Sêr Cymru NRN Fund (NRN097, United Kingdom); the National Natural Science Foundation of China (No.61571429 and 61801464, China).

Appendix A. Supporting material

Supplementary data associated with this article can be found in the attached file.

References

Abbas, A. N., Liu, B., Chen, L., Ma, Y., Cong, S., Aroonyadet, N., Köpf, M., Nilges, T., Zhou, C., 2015. ACS nano 9, 5618-5624.
Acero Sánchez, J.L., Fragoso, A., Joda, H., Suarez, G., McNeil, C.J., O'Sullivan, C. K., 2016. Anal. Bioanal. Chem. 408, 5337-5346.
Bao, Q., Zhang, H., Wang, Y., Ni, Z. H., Yan, Y. L., Shen, Z. X., Loh, K. P., Tang, D. Y., 2009. Adv. Funct. Mater. 19, 3077-3083.
Bao, Q., Zhang, H., Wang, B., Ni, Z., Lim, C. H. Y. X., Wang, Y., Tang, D. Y., Loh, K. P., 2011. Nat. Photon. 5, 411-415.
Bonaccorso, F., Sun, Z., Hasan, T., Ferrari, A. C., 2010. Nature Photon. 4, 611-622.
Caucheteur, C., Guo, T., Liu, F., Guan, B. O., Albert, J., 2016. Nat. Commun. 7, 13371.
Chiavaioli, F., Baldini, F., Tombelli, S., Trono, C., Giannetti, A., 2017. Nanophotonics 6(4), 663-679.
Choi, J. R., Yong, K. W., Choi, J. Y., Nilghaz, A., Lin Y., Xu, J, Lu, X.,2018. Theranostics 8(4), 1005-1026.
Coelho, L., Viegas, D., Santos, J. L. , de Almeida, J. M. M. M., 2016. Sens. Actuators B 223, 45-51.
Cusano, A., Consales, M., Crescitelli, A., Ricciardi A., (Eds.) Lab-on-Fiber Technology. (Springer 2014).
Del Villar, I. Matias, I. R., Arregui, F. J., Lalanne, P., 2005. Opt. Express 13, 56-69.
Dhanabalan, S. C., Ponraj, J. S., Guo, Z., Li, S., Bao, Q., Zhang, H., 2017. Adv. Sci. 4, 1600305.
Erdogan, T., 1997. J. Opt. Soc. Am. A 14, 1760-1773.
Geim, A. K., 2009. Science 324, 1530-1534.
Hanlon, D., Backes, C., Doherty, E., et al., 2016. Nat. Commun. 6, 8563.
Hermanson G. T., Bioconjugate techniques (Third edition), (Academic Press, 2013).
Huang, X., Zeng, Z., Zhang, H., 2013. Chem. Soc. Rev. 42, 1934-1946.
Isgrò, M. A., Bottoni, P., Scatena, R., Advances in cancer biomarkers. R. Scatena (eds), (Springer, 125-143, 2015).
James, S. W. and Tatam, R. P., 2013. Meas. Sci. Technol. 14, R49-R61.
Jiang, B., Yin, G., Zhou, K., Wang, C., Gan, X., Zhao, J., Zhang, L., 2016. Opt. Lett. 41, 5450-5453.
Kim, J., Baik, S. S., Ryu, S. H., Sohn, Y., Park, S., Park, B. G., Denlinger, J., Yi, Y., Choi, H. J., Sim, K. S., 2015. Science 349, 723-726.
Koopal, L. K., Vanriemsdijk, W. H., Dewit, J. C. M., Benedetti, M. F., 1994. J. Colloid Interf. Sci. 166, 51-60.
Kumar, V., Brent, J. R., Shorie, M. et al., 2016. ACS Appl. Mater. Interfaces 8, 22860-22868.
Lee, B. H., Liu, Y., Lee, S. B., Choi, S. S., Jang, J. N., 1997. Opt. Lett. 22, 1769-1771.
Lepinay, S., Staff, A., Ianoul, A., Albert, J., 2014. Biosens. Bioelectron. 52, 337-344.
Li, L., Yu, Y., Ye, G. J., Ge, Q., Ou, X., Wu, H., Feng, D., Chen, X. H., Zhang, Y., 2014. Nat. Nanotechnol. 9, 372-377.
Li, P., Zhang, D., Liu, J., Chang, H., Sun, Y., Yin N., 2015. ACS Appl. Mater. Interfaces 7, 24396-24402.
Liu, C., Cai, Q., Xu, B., Zhu, W., Zhang, L., Zhao, J., Chen, X., 2017. Biosens. Bioelectron. 94, 200-206.
Liu, C., Sun, Z., Zhang, L., Lv, J., Yu, X., Zhang, L., Chen, X., 2018. Sens. Actuators B 257, 1093-1098.
Liu, H., Neal, A. T., Zhu, Z., Xu, X., Tomanek, D., Ye, P. D., 2014. ACS Nano 8, 4033-4041.
Loh, K. P., Bao, Q., Eda, G., Chhowalla, M., 2010. Nat. Chem. 2, 1015-1024.
Nakatsuka, N., Yang, K.-A., Abendroth, J. M., Cheung, K., Xu, X., Yang, H., Zhao, C., Zhu, B., Rim, Y. S., Yang, Y., Weiss, P. S., Stojanović, M. N., Andrews, A. M., 2018. Science eaao6750.
Novoselov, K. S., Geim, A. K., Morozov, S. V., Jiang, D., Zhang, Y., Dubonos, S. V., Grigorieva, I. V., Firsov, A. A., 2004. Science 306, 666-669.
Qu, F. L., Li, T., Yang, M. H., 2011. Biosens. Bioelectron. 26, 3927-3931.
Reich, E. S., 2014. Nature 506, 19.
Rodin, A. S., Carvalho, A., Castro Neto, A. H., 2014. Phys. Rev. Lett. 112, 176801.
Shan, C., Yang, H., Han, D., Zhang, Q., Ivaska, A., Niu, L., 2009. Langmuir 25, 12030-12033.
Shao, J., Xie, H., Huang, H., Li, Z., Sun, Z., Xu, Y., Xiao, Q., Yu, X. F., Zhao, Y., Zhang, H., Wang, H., Chu, P. K., 2016. Nat. Commun. 7, 12967.
Sun, Z., Martinez, A., Wang, F., 2016. Nature Photon. 10, 227-238.
Sun, Z., Xie, H., Tang, S., Yu, X. F., Guo, Z., Shao, J., Zhang, H., Huang, H., Wang, H., Chu, P. K., 2015. Angew. Chem. 127, 11688-11692.
Tan, Y. C., Ji, W. B., Mamidala, V., Chow, K. K., Tjin, S. C., 2014. Sens. Actuators B 196, 260-264.
Van Meerbeeck, J. P., Fennell, D. A., De Ruysscher, D. K. M., 2011. The Lancet 378, 1741-1755.
Wang, X. D. and Wolfbeis, O. S., 2013. Anal. Chem. 85, 487-508.
Wang, R., Wang, G., Zhang, N., Li, X., Liu, Y., 2013. Biomed. Res. Int. 2013, 195692.
Xia, F., Wang, H., Jia, Y., 2014. Nat. Commun. 5, 4458.
Zhou, K., Zhang, L., Chen, X., Bennion, I., 2006. J. Lightw. Technol. 24, 5087-5094.
Zhou, W. H., Zhu, C. L., Lu, C. H., Guo, X. C., Chen, F. R., Yang, H. H., Wang, X. R., 2009. Chem. Commun. 44, 6845-6847.